SEMICONDUCTORS

Room-temperature wavelike exciton transport in a van der Waals superatomic semiconductor

Jakhangirkhodja A. Tulyagankhodjaev, Petra Shih†, Jessica Yu†, Jake C. Russell, Daniel G. Chica, Michelle E. Reynoso, Haowen Su, Athena C. Stenor, Xavier Roy, Timothy C. Berkelbach, Milan Delor*

The transport of energy and information in semiconductors is limited by scattering between electronic carriers and lattice phonons, resulting in diffusive and lossy transport that curtails all semiconductor technologies. Using Re₆Se₈Cl₂, a van der Waals (vdW) superatomic semiconductor, we demonstrate the formation of acoustic exciton-polarons, an electronic quasiparticle shielded from phonon scattering. We directly imaged polaron transport in Re₆Se₈Cl₂ at room temperature, revealing quasi-ballistic, wavelike propagation sustained for a nanosecond and several micrometers. Shielded polaron transport leads to electronic energy propagation lengths orders of magnitude greater than in other vdW semiconductors, exceeding even silicon over a nanosecond. We propose that, counterintuitively, quasiflat electronic bands and strong exciton-acoustic phonon coupling are together responsible for the transport properties of Re₆Se₈Cl₂, establishing a path to ballistic room-temperature semiconductors.

emiconductor technologies rely on transporting energy and information carriers, often in the form of electrons or excitons (bound electron-hole pairs), from source to target. At room temperature, these carriers rapidly scatter with lattice vibrations (phonons) on nanometer and femtosecond scales. Scattering leads to electronic energy dissipation, joule heating, and loss of phase coherence and directionality, imposing strict speed and efficiency limits on all semiconductor technologies. Breaking through these limits requires semiconductors that sustain ballistic (scatterfree), wavelike flow of energy over macroscopic distances at room temperature, a long-sought goal that would enable ballistic transistors (1), low-loss energy harvesting, and wave-based information technologies (2).

Here, we demonstrate macroscopic, wavelike exciton flow at room temperature in the van der Waals (vdW) superatomic material Re₆Se₈Cl₂ (Fig. 1A). Re₆Se₈Cl₂ is a semiconductor with an indirect bandgap of 1.6 eV and an exciton binding energy of ~100 meV (3). Its superatom building blocks consist of Re₆ octahedra enclosed in Se₈ cubes. Each Re₆Se₈ unit is covalently bonded to four neighbors to form a two-dimensional (2D) pseudosquare lattice capped by Cl atoms at the apical positions. The Re₆Se₈Cl₂ layers stack out of plane to create a bulk vdW crystal with weak interlayer electronic coupling (4). The crystal can be exfoliated to the monolayer limit, which is advantageous for integration in gated devices (3, 5, 6). Re₆Se₈Cl₂ exhibits relatively weak intercluster electronic coupling, as evidenced by the electronic band structure (Fig. 1B) (3, 7). Strong coupling of electrons to intercluster optical at room temperature, currently limited only by crystal size. Our observations challenge the common notion that strong electronic coupling is required for long-range transport. Exciton transport in Re₆Se₈Cl₂ is quasi-ballistic We directly imaged exciton transport in singlecrystal Re₆Se₈Cl₂ using ultrafast stroboscopic scattering microscopy (stroboSCAT) (10-12) (Fig. 1D and figs. S1 to S3). An above-gap, diffraction-limited visible pump generates

excitons, and then a backscattering widefield probe (1.55 eV) slightly below the electronic bandgap spatially resolves how the excitons modify the local polarizability of the material. By varying the pump-probe time delay, we spatiotemporally tracked the evolution of photoexcitations in an all-optical, noninvasive, and contact-free measurement. Figure 1E and movie S1 display representative stroboSCAT data obtained in a 60-nm-thick Re₆Se₈Cl₂ flake prepared by mechanical exfoliation (13). Two key features emerge from these data: First, the initial negative (dark) stroboSCAT contrast turns to positive (bright) contrast on picosecond timescales, which, as discussed below (Fig. 2), represents a transition from a bare exciton to an exciton-polaron. Second, the exciton-polaron propagates several micrometers to the edge of

the flake in less than a nanosecond. This very

phonons (8) leads to further band flattening

at room temperature (7) and has been impli-

cated in the emergence of superconductivity

in this material and related classes (6, 9). In

this work, we demonstrate that these quasi-flat

electronic bands, in combination with strong

coupling to acoustic phonons, lead to the for-

mation of acoustic exciton-polarons (Fig. 1C),

quasiparticles of excitons bound to an acoustic

lattice deformation. Through direct imaging

of polaron propagation, we reveal that they are

shielded from lattice scattering, leading to quasi-

ballistic transport over several micrometers

fast and long-range transport differs sta Check for from exciton transport in other molecular o semiconductors (table S1). For comparison, Fig. 1F displays stroboSCAT data of exciton transport in the archetypal vdW semiconductor WSe_2 (bilayer flake on glass; see fig. S4 for monolayer and bulk data), exhibiting much slower and shorter-range transport. These results are counterintuitive, given that the effective mass of excitons in WSe₂ is much smaller than in Re₆Se₈Cl₂ (table S1).

To quantify and rationalize the exceptional transport properties of Re₆Se₈Cl₂, we plotted the mean squared displacement (MSD) of the photoexcited population profile observed in stroboSCAT as MSD = $\sigma^2(t) - \sigma^2(0)$, where σ is the Gaussian width of the population density profile at time delay t (13). Figure 1G compares the MSD for exciton-polarons in Re₆Se₈Cl₂ against the MSD for excitons in bilayer WSe₂ and charge carriers in intrinsic monocrystalline Si (14), which exhibit some of the best transport among 2D and 3D semiconductors, respectively. We find that the MSD at 1.1 ns in Re₆Se₈Cl₂ is 23 times that in bulk WSe₂, 65 times that in bilayer WSe₂, 120 times that in monolayer WSe2, and almost twice that of electrons in intrinsic Si and the recently reported cubic boron arsenide (15, 16) (table S1). On the basis of the 11-ns polaron lifetime (fig. S5), we estimate that the polaron propagation length in Re₆Se₈Cl₂ would exceed 25 µm in the absence of crystal boundaries.

The superlinear behavior of the MSD for Re₆Se₈Cl₂ differs from the linear behavior in Si and WSe₂. We fit the MSD to a power law, MSD $\propto t^{\alpha}$ (11, 12, 17). In the limit of diffusive transport, where scattering lengths are much shorter than the propagation length, $\alpha = 1$. This regime, exemplified by the linear MSD for Si and WSe₂ in Fig. 1F, is observed in virtually all semiconductors beyond the first few femtoseconds after photoexcitation (18). In the limit of coherent, ballistic transport (no scattering), α = 2, meaning that distance is proportional to time with a slope that defines the velocity. In Re₆Se₈Cl₂, we observe quasi-ballistic transport $(\alpha = 1.67 \pm 0.13)$ (Fig. 1G) sustained for nanoseconds, until the flake edge is reached. Plotting the same data as distance versus time provides an effective propagation velocity of 2.3 km/s (fig. S6). Monte Carlo simulations reproducing the observed MSD yield an excitonlattice scattering time of 215 ps, indicating an extraordinary mean free path between scattering events exceeding 1 um for exciton-polarons in Re₆Se₈Cl₂ (Fig. 1H; see figs. S7 and S8 for simulation details and alternative models). These findings reveal that the mechanism for fast and long-range transport in Re₆Se₈Cl₂ is efficient shielding from scattering, amply compensating for the large effective mass (and thus low intrinsic velocity) of the polaron. These results are reproducible in multiple flakes of different

Department of Chemistry, Columbia University, New York, NY

^{*}Corresponding author. Email: milan.delor@columbia.edu †These authors contributed equally to this work.

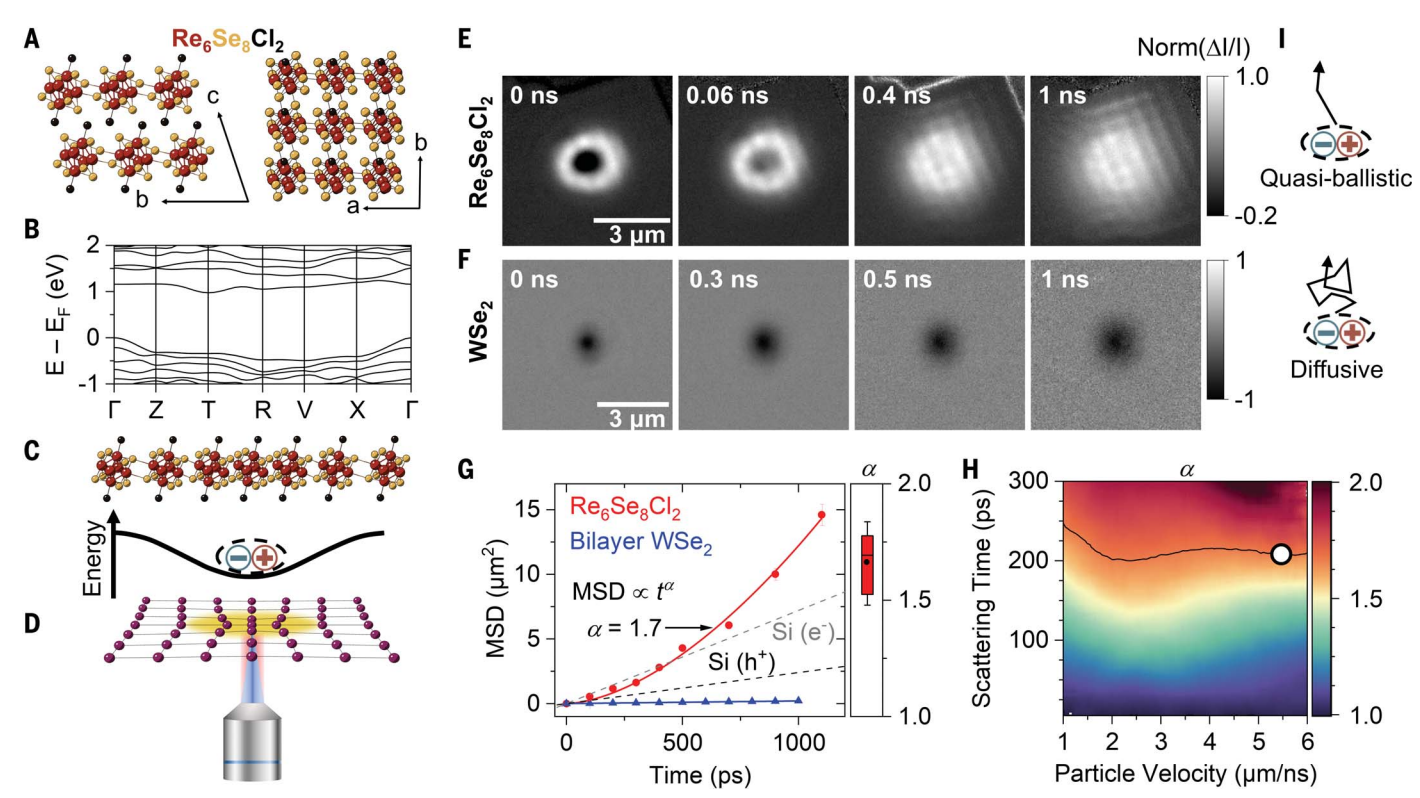


Fig. 1. Imaging exciton transport in Re₆Se₈Cl₂. **(A)** Crystal structure of Re₆Se₈Cl₂. **(B)** Band structure of Re
6Se₈Cl₂ calculated using density functional theory with the Perdew-Burke-Ernzerhof (PBE) exchange correlation functional (13). **(C)** Formation of acoustic polarons through a deformation potential interaction. **(D)** Schematic for optical far-field imaging of polaron transport (details in the text and figs. S1 to S3). **(E)** Picosecond stroboSCAT time series displaying exciton (dark contrast) and exciton-polaron (bright contrast) propagation in a 60-nm-thick Re
6Se₈Cl₂ flake on glass. ΔII refers to the pump-induced change in backscattered light intensity. **(F)** Exciton propagation in bilayer WSe₂ on glass. **(G)** Mean squared displacement (MSD) of exciton-polarons in Re
6Se₈Cl₂ (red), excitons in WSe₂

(blue), and charge carriers in Si (gray and black). Error bars are 1 SD. Only $Re_6Se_8Cl_2$ displays superlinear behavior, indicating superdiffusive transport characterized by the exponent $\alpha.$ The box plot shows the spread of α values across 11 different datasets, indicating mean and median values of 1.67 and 1.7, respectively. (**H**) Monte Carlo simulation of α for different particle velocities (v) and scattering times (τ) for our experimental configuration. The circle corresponds to simulation parameters of ν = 5.5 km/s and τ = 215 ps that reproduce the experimental MSD. The black contour traces α = 1.67. (**I**) Illustration of quasi-ballistic motion of polarons in $Re_6Se_8Cl_2$ compared with diffusive motion for excitons in WSe2 and other semiconductors. Data acquired at 295 K.

thicknesses (Figs. 1 and 3), for both above-gap and band-edge pump excitation (fig. S9), for pump temporal pulse widths spanning 60 fs to 60 ps (fig. S10), and across a range of fluences explored in detail below (Fig. 3), indicating that neither hot carrier transport (19), phonon winds (20, 21), nonlinear recombination (22), thermal gradients (23), nor strain waves (24–27) are responsible for the observed behavior (figs. S9 to S12 and table S2).

Excitons in Re₆Se₈Cl₂ form exciton-polarons

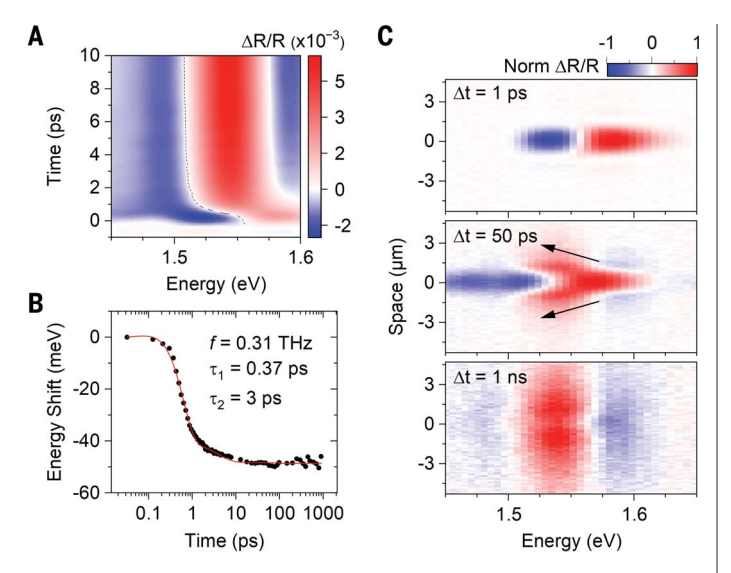
To confirm that polaron formation is responsible for the observed transport behavior, we tracked the energetic evolution of excitons after photoexcitation and correlated these dynamics to optical transport measurements. Figure 2A displays transient reflectance spectra in the region of the semiconductor band edge, exhibiting a bleach around 1.57 eV and a photoinduced absorption ~90 meV higher in energy. The primary dynamic evolution observed is a spectral redshift on a 1.5-ps timescale that convolves all peaks. Identical dynamics are observed for near-band-edge excitation (fig. S9), ruling out

the possibility that electronic thermalization is responsible for the redshift. Tracking the zerocrossing of the transient reflectance profile (dashed line in Fig. 2A) provides a handle on redshift kinetics, plotted in Fig. 2B. We observe an overall 48 meV redshift with an evolution resembling a strongly damped oscillator (red line in Fig. 2B). These dynamics echo those previously observed for (large) polaron formation (28-31), wherein energetic stabilization occurs over a single vibrational period of the associated lattice deformation. This spectral evolution is responsible for the switch from dark to bright contrast in stroboSCAT in Fig. 1E: The probe at 1.55 eV is initially pre-resonant with the exciton transition (dark contrast) but switches to resonant with the induced polaron absorption after the redshift, generating a bright contrast (additional stroboSCAT datasets at different probe wavelengths are displayed in fig. S13). Below, we discuss measurements of correlated spatioenergetic dynamics, fluence-dependent redshift dynamics, and population saturation that cement our assignment of these redshift dynamics to polaron formation.

Polarons should exhibit correlated spatial and spectral dynamics, given that energetic stabilization associated with polaron formation results in a modification of transport properties. To directly image these correlated dynamics and further support the correspondence between the redshift timescale and the polaron formation timescale, we developed an approach capable of simultaneously resolving spectral and spatial evolution by merging stroboSCAT with transient reflectance microscopy (fig. S2). Figure 2C displays spatially resolved transient spectra at different pump-probe time delays (see also movies S2 and S3). At early times, the transient reflectance signal associated with excitons is concentrated around the pump excitation location at 0 µm. Between 4 and 50 ps, a V-shaped pattern emerges (highlighted with arrows in Fig. 2C), indicating that the spectral redshift associated with polaron formation is correlated to transport away from the excitation location. By 1 ns, only the redshifted polaron spectral signature remains, showing propagation over several micrometers. The correlated spatioenergetic dynamics are a clear indication that

Fig. 2. Spatio-energetic tracking of polaron formation in Re₆Se₈Cl₂.

(A) Transient reflectance spectra near the band edge after 2.41 eV pump excitation at an initial exciton density of $5 \times 10^{17} / \text{cm}^3$. $\Delta R / R$ refers to the pumpinduced change in reflected light intensity. (B) Trace of the redshift highlighted with a dashed line in (A). The red line is a fit using a damped oscillator model with a frequency of 0.31 THz and damping time of 0.37 ps, combined with a



3-ps exponential decay. **(C)** Spacetime-transient reflection spectra after 2.41 eV pump excitation at an initial exciton density of $8 \times 10^{18}/\text{cm}^3$ for three time delays. The correlated redshift and transport dynamics are emphasized with arrows in the middle panel. Movies S2 and S3 display these coupled spatio-energetic dynamics for different excitation fluences. Data acquired at 295 K.

excitons in ${\rm Re_6Se_8Cl_2}$ become substantially mobile only after they have formed exciton-polarons; bare excitons are effectively immobile, whereas polarons propagate over micrometers. The observed transport dynamics also rule out traditional exciton self-trapping (small polarons), which would reduce the exciton mobility upon polaron formation (32). These results illustrate the power of our correlative approach for understanding how polaron formation affects transport.

Finally, we confirmed the formation of polarons in Re₆Se₈Cl₂ and experimentally inferred their size by determining the density at which they begin to interact. At high densities, lattice deformations compete to displace the same atoms, resulting in a diminished ability to form polarons (Fig. 3A) (32). stroboSCAT data displayed in Fig. 3B shows that as the photoexcitation density increases, the bare exciton signal (dark contrast) begins to dominate over the polaron signal (bright contrast), indicating that polaron formation is suppressed in regions of high excitation density. Figure 3C compares the polaron population (red trace) and bare exciton population (black trace) as a function of excitation fluence (analysis in fig. S14). We observed clear saturation of the polaron population at exciton densities between $0.45 \times 10^{18} \text{/cm}^3$ and $1.8 \times 10^{18} \text{/cm}^3$ (highlighted) with a blue rectangle). This behavior signals that polarons are overlapping in space, analogous to a Mott transition that prevents further polaron formation (33). The onset of polaron saturation is also reflected in a transition from superdiffusive to almost diffusive transport (Fig. 3D), which we attribute to polaron-polaron scattering above the saturation density. The suppression of exciton-to-polaron conversion above saturation is most evident in the spectral dynamics (Fig. 3E and fig. S15), where the redshift time associated with exciton stabilization increases from ~1.5 ps to hundreds of picoseconds. We reproduced these spectral dynamics (right panels of Fig. 3E) with a saturation model accounting for a kinetic blockade and polaron transport away from the excitation area (figs. S15 and S16). According to the Mott criterion (34), the polaron interaction radius associated with the observed critical density range of $0.45 \times 10^{18}/\text{cm}^3$ to $1.8 \times 10^{18}/\text{cm}^3$ is 2.1 to 3.4 nm, corresponding to three- to five-unit cells in Re₆Se₈Cl₂.

Acoustic polarons are responsible for wavelike transport

Large polarons, known to form in materials such as lead halide perovskite semiconductors, have been suggested to partially shield carrier-lattice scattering (35). Nevertheless, experiments consistently demonstrate a diffusive transport regime (10, 18, 19, 36), with sub-100-fs scattering times that indicate insufficient shielding to switch into the much-desired macroscopic ballistic transport regime. In contrast, the sustained quasi-ballistic behavior observed in Re₆Se₈Cl₂ is reminiscent of acoustic polarons, which can form in low-dimensional materials and were theoretically invoked to rationalize the transport properties of polydiacetylene in one dimension (37, 38).

The formation of acoustic polarons is rare, as is our observation of micrometer-scale exciton mean free paths at room temperature. To rationalize this notable behavior in ${\rm Re_6Se_8Cl_2}$, we use an approximate strong-coupling theory that describes an exciton of mass m coupled to acoustic phonons with a strength quantified by the deformation potential D in two dimensions. The acoustic phonons derive from superatoms

of mass M with intercluster vibrational frequency Ω . In two dimensions, the energy to form a circular polaron with radius a and area πa^2 is

$$E = \frac{\hbar^2}{2ma^2} + \frac{1}{2}M\Omega^2\Delta^2\pi a^2 - D\Delta \qquad (1)$$

where Δ is the dimensionless lattice displacement and \hbar is the reduced Planck constant (39). In this simple picture, the polaron is only bound if the electron–phonon interaction outweighs the energetic penalties associated with exciton localization and lattice deformation. Minimizing Eq. 1 with respect to the lattice displacement Δ gives the existence criterion

$$\begin{split} \lambda > \lambda_{\rm c}, \lambda &= \frac{mD^2}{2\hbar^2 M \Omega^2} = \frac{D^2}{4JMs^2}, \\ \lambda_{\rm c} &= {}^\pi/{}_2 \approx 1.6 \end{split} \tag{2}$$

where λ is a dimensionless measure of the exciton-acoustic phonon coupling strength, and in the second equality we have introduced the exciton transfer integral J and the speed of sound $s = \Omega a$. Applying density functional theory to Re₆Se₈Cl₂, we calculate D = 4.4 eV (13). Taking into account the experimentally inferred electronic band flattening due to intercluster optical phonons, which increases the exciton effective mass from $1.9m_e$ at 0 K to $60m_e$ at 300 K (7), we calculate a very small J of 1.5 meV at 300 K (13). When combined with the other material parameters (table S3), we find that $\lambda = 7 > \lambda_c$, predicting a strongly bound polaron. Figure 4A plots the coupling strength λ for Re₆Se₈Cl₂, monolayer WSe2, crystalline pentacene, and 2D organic-inorganic halide perovskites. Re₆Se₈Cl₂ has a coupling strength λ that is 10 to 1000 times greater than that of the other materials and is thus the only material considered in Fig. 4 that is predicted to exhibit bound acoustic polarons according to the criterion in Eq. 2. Within this theory, the key parameters setting Re₆Se₈Cl₂ apart from other 2D and 3D semiconductors is the combination of a quasi-flat electronic band structure at room temperature (small J) and strong exciton-acoustic phonon interactions (large D), yielding a large coupling strength λ and associated strongly bound acoustic polarons. The polaron binding energy is reduced with decreasing temperature owing to the increase in the transfer integral J(7, 13). The estimate in Eq. 2 predicts that the polaron is not bound below ~175 K. Temperature-dependent stroboSCAT experiments (fig. S17) display a drastic reduction in MSD below ~150 K, lending support to our central hypothesis and theory of acoustic polarons. We emphasize that Eq. 2 only provides a qualitative criterion for polaron formation and a detailed understanding of the polaron stability and lifetime at finite temperature requires a more complete theoretical treatment (13).

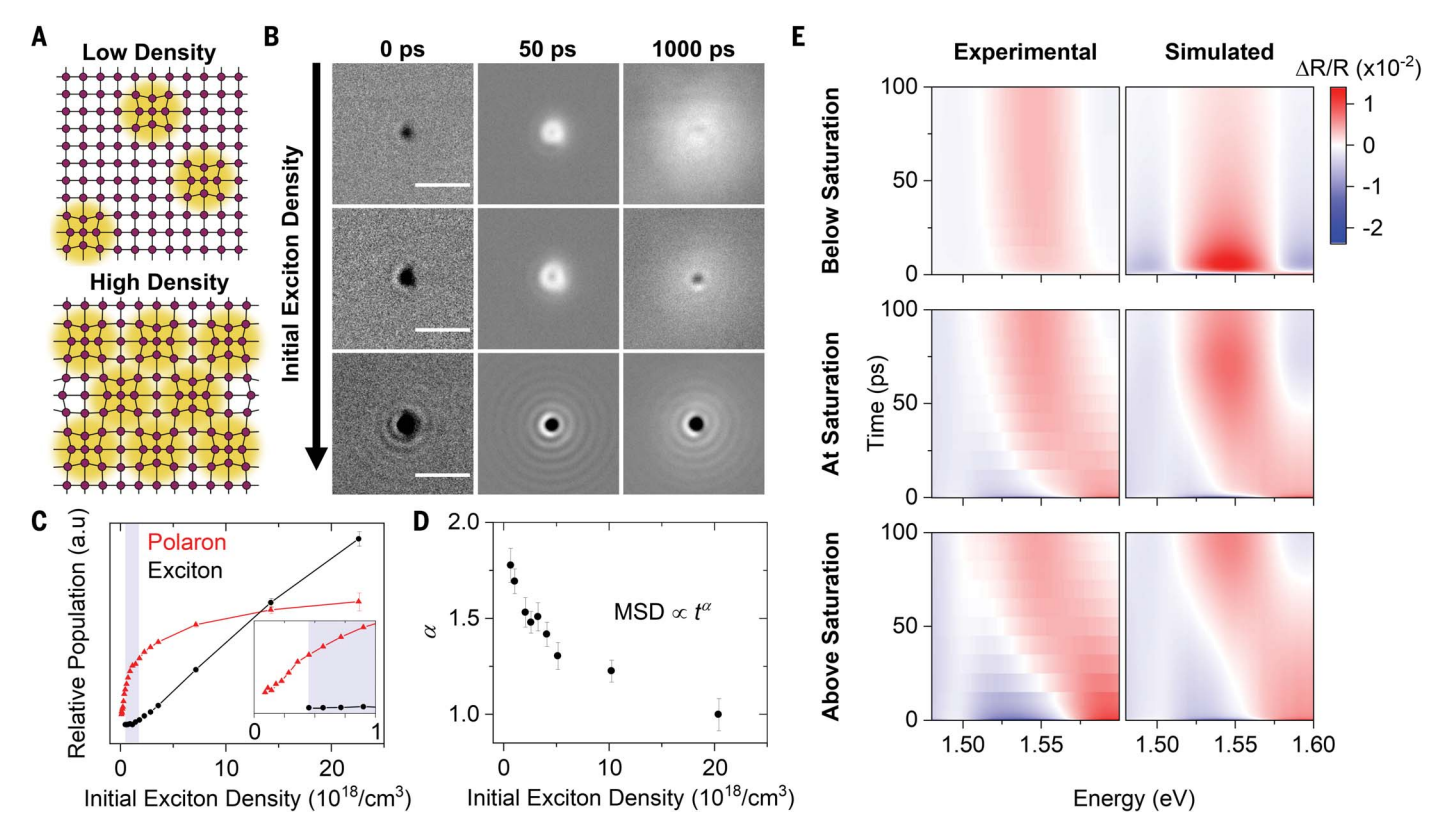
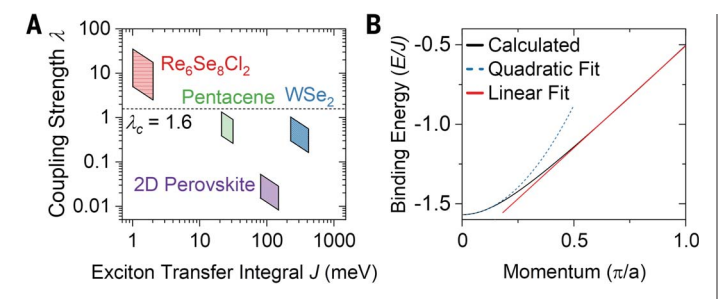


Fig. 3. Determining polaron size in Re₆Se₈Cl₂. **(A)** Depiction of polaron blockade at high densities. **(B)** Femtosecond stroboSCAT images at pump/probe energies of 2.41 eV/1.55 eV at initial exciton densities ranging from $1 \times 10^{18}/\text{cm}^3$ to $20 \times 10^{18}/\text{cm}^3$ in a 350-nm-thick Re₆Se₈Cl₂ flake on glass. Bare excitons are associated with dark contrast, whereas polarons are associated with bright contrast. The rings observed at high exciton densities are diffraction rings. All scale bars are 3 μ m. **(C)** Relative populations of polarons and bare excitons at a pump-probe time delay of 5 ps as a function of initial exciton density, indicating saturation

of the polaron population. The blue shaded region for exciton densities between $0.45 \times 10^{18}/\text{cm}^3$ and $1.8 \times 10^{18}/\text{cm}^3$ indicates the range of critical polaron overlap density. (**D**) MSD exponent, α , as a function of initial exciton density. Error bars are 1 SD. (**E**) Experimental (left) and simulated (right) transient reflectance spectra taken at the center of the focused pump excitation (B) for different initial exciton densities. Simulations are based on a saturation model accounting for exciton-to-polaron conversion and polaron transport away from the excitation spot (13). Data acquired at 295 K.

Fig. 4. Energy of an acoustic polaron.

(A) The coupling strength λ for different systems, presented as a function of their exciton transfer integral J. The boxed regions represent the upper and lower bounds for a range of deformation potentials and exciton



transfer integrals within 30% of reported data (material properties collected in table S3). The critical value of λ_c = 1.6 is plotted as a dashed line. (**B**) Calculated polaron dispersion for Re₆Se₈Cl₂ (*13*). The band effective mass is estimated by a parabolic fit at the minimum (dashed blue line). The solid red line emphasizes the linearity of the dispersion for higher values of momentum.

Rationalizing the quasi-ballistic dynamics of acoustic polarons requires a more sophisticated quantum mechanical treatment. We generalize the stationary polaron description above and propose a variational wave function for the moving polaron defined by its average crystal momentum (13). Energy minimization produces the polaron dispersion shown in Fig. 4B. Near the band bottom, we extract a large

effective polaron mass $m^* \approx 200 m_e$, a substantial increase from the bare exciton mass of $60 m_e$ at 300 K. More importantly, at higher momenta, the polaron inherits the linear dispersion of acoustic phonons—a renormalization evocative of light–matter hybridization to form polaritons (40). The linear dispersion of acoustic polarons with a slope below that of other acoustic phonons implies weak scattering because

there are no dissipation channels that conserve both energy and momentum (38). The polaron is thus predicted to move quasi-ballistically at a speed proportional to the speed of sound of the lattice, consistent with our experimental observations.

Discussion and outlook

We have observed a transport regime mediated by acoustic exciton-polarons in the vdW superatomic semiconductor Re₆Se₈Cl₂. Polaron formation shields excitons from scattering with lattice phonons, resulting in quasi-ballistic electronic energy flow over several micrometers within a nanosecond at room temperature. We reveal a very long exciton mean free path of ~1 µm, suggesting the possibility of ballistic excitonic transistors. Our discovery of this regime in a material with weak electronic dispersion provides an alternative to the current paradigm of increasing electronic conjugation to improve transport. Indeed, our model for 2D acoustic polarons suggests that quasi-flat electronic bands and strong electron-phonon interactions can counterintuitively result in exceptional electronic transport. Beyond 2D superatomic materials such as $\mathrm{Re}_0\mathrm{Se}_8\mathrm{Cl}_2$ and the recently reported graphullerene (41), moiré superlattices of 2D semiconductors may provide an interesting testing ground for acoustic polarons. Their superlattice potentials enable tuning electronic bands (42, 43) to achieve values of J down to ~0. Combined with their strong deformation potentials (44), these flat bands could yield acoustic polarons with tunable transport properties across a large temperature range. Generalizing wavelike, ultralong-range electronic energy flow in 2D materials could herald an era of essentially lossless nanoelectronics.

REFERENCES AND NOTES

- A. Javey, J. Guo, Q. Wang, M. Lundstrom, H. Dai, *Nature* 424, 654–657 (2003).
- 2. G. D. Scholes et al., Nature 543, 647-656 (2017).
- 3. X. Zhong et al., Nano Lett. 18, 1483-1488 (2018).
- 4. B. Choi et al., J. Am. Chem. Soc. 140, 9369-9373 (2018).
- 5. E. A. Doud et al., Nat. Rev. Mater. 5, 371-387 (2020).
- 6. E. J. Telford et al., Nano Lett. 20, 1718-1724 (2020).
- Q. Li, F. Liu, J. C. Russell, X. Roy, X. Zhu, J. Chem. Phys. 152, 171101 (2020).
- 8. K. Lee et al., Adv. Mater. 31, e1903209 (2019).
- 9. J. Chen, A. J. Millis, D. R. Reichman, *Phys. Rev. Mater.* 2, 114801 (2018).
- M. Delor, H. L. Weaver, Q. Yu, N. S. Ginsberg, *Nat. Mater.* 19, 56–62 (2020).
- T. Zhu, J. M. Snaider, L. Yuan, L. Huang, Annu. Rev. Phys. Chem. 70, 219–244 (2019).
- 12. N. S. Ginsberg, W. A. Tisdale, Annu. Rev. Phys. Chem. 71, 1-30 (2020).
- 13. Materials and methods are available as supplementary materials. 14. C. Jacoboni, C. Canali, G. Ottaviani, A. Alberigi Quaranta,
- 14. C. Jacoboni, C. Canali, G. Ottaviani, A. Alberigi Quaranta, *Solid-State Electron.* **20**, 77–89 (1977).
- 15. J. Shin et al., Science 377, 437-440 (2022).
- 16. S. Yue et al., Science 377, 433-436 (2022).
- 17. G. M. Akselrod et al., Nat. Commun. 5, 3646 (2014).

- 18. J. Sung et al., Nat. Phys. 16, 171-176 (2020).
- 19. Z. Guo et al., Science 356, 59-62 (2017).
- 20. M. M. Glazov, Phys. Rev. B 100, 045426 (2019).
- 21. L. M. Smith et al., Phys. Rev. B 39, 1862–1870 (1989).
- 22. M. Kulig et al., Phys. Rev. Lett. 120, 207401 (2018).
- 23. R. Perea-Causín et al., Nano Lett. 19, 7317-7323 (2019).
- P. Ruello, V. E. Gusev, *Ultrasonics* **56**, 21–35 (2015).
 J. Rudolph, R. Hey, P. V. Santos, *Phys. Rev. Lett.* **99**, 047602 (2007).
- 26. E. Baldini et al., Sci. Adv. 5, eaax2937 (2019).
- 27. K. Datta et al., Nat. Photonics 16, 242–247 (2022).
- 28. K. Miyata et al., Sci. Adv. 3, e1701217 (2017).
- F. X. Morrissey, J. G. Mance, A. D. Van Pelt, S. L. Dexheimer, J. Phys. Condens. Matter 25, 144204 (2013).
- 30. B. Guzelturk et al., Nat. Mater. 20, 618-623 (2021).
- 31. B. Wu et al., Sci. Adv. 7, eabd3160 (2021).
- 32. D. Emin, Polarons (Cambridge Univ. Press, 2012).
- J. M. Frost, L. D. Whalley, A. Walsh, ACS Energy Lett. 2, 2647–2652 (2017).
- 34. P. P. Edwards, M. J. Sienko, Phys. Rev. B 17, 2575-2581 (1978).
- 35. H. Zhu et al., Science 353, 1409-1413 (2016).
- Z. Guo, J. S. Manser, Y. Wan, P. V. Kamat, L. Huang, Nat. Commun. 6, 7471–7479 (2015).
- 37. H.-B. Schüttler, T. Holstein, Phys. Rev. Lett. 51, 2337-2340 (1983).
- 38. E. G. Wilson, J. Phys. C Solid State Phys. 16, 6739-6755 (1983).
- 39. G. Whitfield, P. B. Shaw, Phys. Rev. B 14, 3346-3355 (1976).
- 40. D. L. Mills, E. Burstein, Rep. Prog. Phys. 37, 817–926 (1974).
- 41. E. Meirzadeh et al., Nature 613, 71-76 (2023).
- 42. L. Wang et al., Nat. Mater. 19, 861-866 (2020).
- F. Wu, T. Lovorn, E. Tutuc, A. H. MacDonald, *Phys. Rev. Lett.* 121, 026402 (2018).
- 44. D. Waters et al., ACS Nano 14, 7564-7573 (2020)
- J. Tulyagankhodjaev et al., Dataset for "Room temperature wavelike exciton transport in a van der Waals superatomic semiconductor," version 1, Zenodo (2023); https://doi.org/10.5281/zenodo.8183811.

ACKNOWLEDGMENTS

We are grateful to P. Batail for bringing this family of materials to our attention and for ensuing productive discussions. We also thank L. E. Brus, X. Zhu, C. Nuckolls, and D. R. Reichman for helpful discussions and D. Xu and J. Baxter for technical help with measurements and analysis. **Funding:** This material is primarily based on work supported by the National Science Foundation

(NSF) through the Columbia MRSEC on Precision-Assembled Quantum Materials (PAQM) (DMR-2011738) (M.D., X.R., and T.C.B.) and by the Air Force Office of Scientific Research (AFOSR) under grant number FA9550-22-1-0389 (M.D. and X.R.). stroboSCAT instrument development was supported by the NSF under grant number DMR-2115625 (M.D.). M.D. acknowledges support from the Arnold and Mabel Beckman Foundation through a Beckman Young Investigator award. X.R. and J.Y. acknowledge support from NSF CAREER Award DMR-1751949, J.A.T. was supported by an NSF Graduate Research Fellowship, J.C.R. was supported by a Department of Defense National Defense Science and Engineering Graduate Fellowship. Author contributions: J.A.T. and M.D. conceived of and designed the experiments. J.A.T performed, analyzed, and simulated stroboSCAT and spacetime transient reflection experiments with assistance from A.C.S. J.Y., J.C.R., D.G.C., and X.R. synthesized and characterized ResSesClo single crystals. J.Y. performed and analyzed heat capacity measurements. J.A.T., M.E.R., J.Y., and H.S. prepared exfoliated samples. P.S. and T.C.B. developed the theory and performed density functional theory calculations and polaron dispersion calculations, M.D. supervised the project, J.A.T., P.S., J.Y., X.R., T.C.B., and M.D. wrote the manuscript, with input from all authors. Competing interests: The authors declare that they have no competing interests. Data and materials availability: All data and code necessary to reproduce the figures in the main text and supplementary materials are available on Zenodo (45). License information: Copyright © 2023 the authors, some rights reserved; exclusive licensee American Association for the Advancement of Science. No claim to original US government works. https://www. science.org/about/science-licenses-journal-article-reuse

SUPPLEMENTARY MATERIALS

science.org/doi/10.1126/science.adf2698 Materials and Methods Supplementary Text Figs. S1 to S17 Tables S1 to S3 References (46–71) Movies S1 to S3

Submitted 11 October 2022; accepted 21 September 2023 10.1126/science.adf2698